# Phonon Thermal Transport in $Bi_2Te_3$ from a Deep-Neural-Network Interatomic Potential

Pan Zhang,[1,2] Zhenhua Zhang,[3] Yong Liu,[1] Ziyu Wang,[2] Zhihong Lu,[3,*] and Rui Xiong[1,†]

[1] *Key Laboratory of Artificial Micro- and Nano-structures of Ministry of Education, School of Physics and Technology, Wuhan University, Wuhan 430072, People's Republic of China*

[2] *Suzhou Institute of Wuhan University, Suzhou 215123, People's Republic of China*

[3] *School of Materials and Metallurgy, Wuhan University of Science and Technology, Wuhan 430081, People's Republic of China*

(Received 22 June 2022; revised 19 September 2022; accepted 29 September 2022; published 8 November 2022)

$Bi_2Te_3$ is a widely used thermoelectric material with strong anharmonicity. Determination of its thermal conductivity requires consideration of the high-order phonon scattering process, which makes it extremely time consuming and challenging to accurately calculate its thermal conductivity by obtaining high-order force constants based on density-functional theory. In this work, a deep-neural-network potential is developed to reproduce phonon dispersion and predict the lattice thermal conductivity of $Bi_2Te_3$. The equilibrium molecular dynamics simulations combined with this potential are performed to calculate the lattice thermal conductivity and the results nicely match the experimental values. Meanwhile, we find the generalized gradient approximation with the DFT-D3 functional can accurately reproduce the experimental lattice constants of $Bi_2Te_3$ and provide a description of the phonon dispersion in $Bi_2Te_3$ as well as the local density approximation. Furthermore, we explore the influence of the native point defects on thermal conductivity, and find that Te vacancies have the most significant effect on the reduction of thermal conductivity, owing to the appreciable inhibition of phonon propagation speed by Te vacancies, and the additional scattering among original low-frequency optical phonons and the fresh low-frequency optical phonons moving downward from high frequency region, which provides some theoretical guidance for reducing thermal conductivity in experimental research.

DOI: 10.1103/PhysRevApplied.18.054022

## I. INTRODUCTION

Addressing the energy challenge has become a significant issue in the world. Since thermoelectric materials can recover waste heat and directly convert it to electricity without any environmental pollution, they have attracted extensive attention and extremely widespread research from scientific researchers in recent decades [1,2]. The traits of a thermoelectric material can be evaluated by the figure of merit $ZT = S^2\delta T/\kappa$, where $S$, $\delta$, $T$, and $\kappa$ represent the Seebeck coefficient, electrical conductivity, temperature, and thermal conductivity, respectively. Here, thermal conductivity contains lattice thermal conductivity $\kappa_l$ and charge-carrier thermal conductivity $\kappa_e$. Generally, a promising thermoelectric material should possess high Seebeck coefficient, high electrical conductivity, and low thermal conductivity to obtain an excellent figure of merit.

$Bi_2Te_3$-based compounds are the most widely used thermoelectric materials with excellent properties near room temperature. Bulk $Bi_2Te_3$ belongs to the $D_{3d}^5$ ($R\bar{3}m$) space group with a tetradymite lattice structure. Every five atomic layers Te1/Bi/Te2/Bi/Te1 make a quantum layer, and the adjacent quantum layers are combined by weak van der Waals (vdW) forces between Te1 atoms, while Te2 atoms are located between two Bi atomic layers. Researchers have strived to further improve its $ZT$ value for decades in the hope that the efficiency of thermoelectric devices can be comparable to that of traditional heat engines. Since the beginning of the 21st century, with the vigorous development of nanotechnology, a great leap has been brought about in the research of thermoelectric materials, including $Bi_2Te_3$. By ball milling and hot pressing of nanoparticles into bulk alloys, a $ZT$ value as high as 1.4 was successfully obtained at 100 °C in $p$-type nanostructured $Bi_xSb_{2-x}Te_3$ [3]. The strong scattering of phonons at the nanostructure boundary leads to a significant decrease in thermal conductivity, which is the crucial reason for $ZT$ enhancement. Another work greatly improved the scattering of intermediate frequency phonons by introducing the dense dislocation arrays in $Bi_{0.5}Sb_{1.5}Te_3$, resulting in a great decrease in thermal conductivity and a peak $ZT$

*Corresponding author. zludavid@live.com
†Corresponding author. xiongrui@whu.edu.cn

 

of 1.86 [4]. In the study of thermoelectric thin films, a *ZT* value of 2.4 was reported in a *p*-type $Bi_2Te_3/Sb_2Te_3$ superlattice, which was also due to achieving an extremely low thermal conductivity of 0.22 W/mK in the cross-plane direction [5,6]. Beyond these, nanotechnology has also been applied to reduce the thermal conductivity of other thermoelectric materials successfully. By introducing full-scale phonon scattering, from atomic scale to mesoscale, a huge reduction in thermal conductivity was achieved and this led to a large enhancement in the thermoelectric performance of PbTe [7]. These works indicate that reducing thermal conductivity is an effective means of improving the *ZT* of $Bi_2Te_3$ and other thermoelectric materials. Therefore, it is important that more efforts should be made to carry out theoretical research on the thermal transport properties of $Bi_2Te_3$-based compounds, especially the influence of nanostructures on its thermal conductivity.

Although the thermoelectric properties of $Bi_2Te_3$ have been widely studied in experiments, the theoretical research on its thermal conductivity is still relatively rare, largely due to its complicated crystal structure and strong anharmonicity. The phonon line shapes of $Bi_2Te_3$ along the high-symmetry paths at different temperatures were calculated in previous work [8], and show a notable broadening of the linewidths and satellite peaks at or above room temperature, directly confirming the anomalous anharmonicity of this material. For materials with strong anharmonicity, the high-order phonon scattering process is critical for the accurate calculation of thermal conductivity [9]. As a consequence, the Boltzmann transport equation (BTE) method overestimated the thermal conductivity of $Bi_2Te_3$ by only considering the three-phonon scattering process [10]. The molecular dynamics (MD) simulation inherently involves four-phonon scattering and higher-order scattering processes, so this method is more suitable for predicting the thermal conductivity of materials with strong anharmonicity. Therefore, a three-body interatomic potential [11] and a Morse potential [12] were developed to calculate the thermal conductivity of $Bi_2Te_3$. However, both of the two empirical potentials would either overestimate or underestimate its lattice thermal conductivity. Hellman *et al.* [8] took a particularly appropriate approach, *ab initio* molecular dynamics (AIMD), which includes all orders of the phonon scattering process, to calculate the thermal conductivity of $Bi_2Te_3$ and the obtained results are in good agreement with experimental values [13]. Unfortunately, this method is very time consuming and is unable to calculate the thermal conductivity of large nanostructures like classical MD can. A high-precision method is urgently needed for the calculation of the thermal conductivities of large systems, so that the effects of nanostructures on the thermal conductivity of $Bi_2Te_3$ can be studied.

The rapid development of machine learning in recent years has brought hope to solving this accuracy-versus-efficiency dilemma [14–18]. A large number of studies using the machine learning potential to calculate thermal conductivity have emerged, making it possible to study the thermal conductivity of some substances, like $\beta$-$Ga_2O_3$ with a large conventional cell [19], $Mn_xGe_y$ materials with a wide range of compositions [20], crystalline and amorphous silicon [21,22], $ZnCl_2$-NaCl-KCl ternary salts [23], complex skutterudite compounds [24,25], etc. In this work, we develop a deep-neural-network potential (NNP) to predict the lattice thermal conductivity of $Bi_2Te_3$ using the equilibrium molecular dynamics (EMD) simulation. The calculated thermal conductivities are in great agreement with experimental values in the temperature range of 150 to 450 K. At the same time, by comparing the thermal conductivities of structures with different kinds of native point defects, our results interestingly show that Te vacancies have the most significant effect on the reduction of thermal conductivity. In addition, it is worth mentioning that we also propose that the generalized gradient approximation (GGA) with DFT-D3 functional can describe the phonon dispersion in $Bi_2Te_3$ as well as the local density approximation (LDA). Moreover, GGA + DFT-D3 calculations can accurately reproduce the experimental lattice constants of $Bi_2Te_3$, compared with any other vdW functionals previously reported.

## II. METHODS

### A. Construction of a deep-neural-network interatomic potential

A training data set and testing data set are respectively prepared for training and testing the NNP (see Sec. III). Calculations of all data sets are carried out using first principles calculations based on density-functional theory (DFT) as implemented in the Vienna *ab initio* simulation package (VASP) [26]. The projector-augmented-wave method [27] and the Perdew-Burke-Ernzerhof (PBE) exchange-correlation functional with GGA [28] are used. The plane-wave energy cutoff is set to 500 eV and the energy convergence threshold employed for AIMD and static self-consistent calculations are set to $10^{-6}$ eV. Considering that the calculated system contains 240 atoms, the Monkhorst-Pack *k*-point meshes are set to $2 \times 2 \times 1$. To describe the interlayer vdW forces, the DFT-D3 functional [29] is also included. We use the so-called PHONOPY [30] package to study the phonon dispersion of $Bi_2Te_3$ with the finite-displacement method. A $3 \times 3 \times 3$ supercell is used to obtain harmonic interatomic force constants with $3 \times 3 \times 3$ *k*-point meshes. The phonon dispersions of structures with native point defects are derived in the same way. A $4 \times 4 \times 1$ conventional supercell with three defects and $3 \times 3 \times 1$ *k*-point meshes are employed.

In this work, the DeePMD-kit package [14] (version 2.0.0) is adopted to train the NNP, in which potential

energy $E$ is equal to the sum of the energies of all atoms,

$$E = E_i. \tag{1}$$

The energy of each atom $E_i$ is completely determined by its the local atomic environment,

$$E_i = E_{s_{(i)}}(R_i, \{R_j | j \in N_{R_c}(i)\}), \tag{2}$$

where $N_{R_c}$ stands for atomic index within the cutoff radius $R_c$, and $s_i$ denotes the chemical species of atom $i$. The coordinate information of individual atoms is constructed by a feature matrix,

$$D_{ij}^{\alpha} = \begin{cases} \left\{\frac{1}{R_{ij}}, \frac{x_{ij}}{R_{ij}}, \frac{y_{ij}}{R_{ij}}, \frac{z_{ij}}{R_{ij}}\right\}, & R_{ij} \le R_{cs}; \\ \left\{\frac{1}{R_{ij}}\right\}, & R_{cs} \le R_{ij} \le R_c. \end{cases} \tag{3}$$

In this training, the embedding and fitting networks are set as {25, 50, 100} and {240, 240, 240}, respectively. Considering that there are two long-range forces in the system, Coulomb force and vdW force, a relatively large cutoff radius of 10 Å for neighbor searching is set. In addition, the prefactors included $p_e^{\text{star}}, p_e^{\text{limit}}, p_f^{\text{star}}, p_f^{\text{limit}}, p_v^{\text{star}}, p_v^{\text{limit}}$ for loss functions are set to 0.02, 8, 1000, 2, 0.8, and 1, respectively. Two million training steps are more than enough to achieve convergence.

### B. Calculation of thermal conductivity

The EMD simulation together with the Green-Kubo formulation [31] is an effective method to calculate the thermal conductivity of solid materials. In this work, all the MD simulations are executed using the large-scale atomic/molecular massively parallel simulator called LAMMPS [32]. According to the Green-Kubo theory, the lattice thermal conductivity is expressed as

$$K_{l,\alpha} = \frac{1}{k_B V T^2} \int \langle J_\alpha(0) \cdot J_\alpha(t) \rangle \, dt, \quad \alpha = x, y, z, \tag{4}$$

where $k_B$ is the Boltzmann constant, $V$ the volume of the simulated system, $T$ the temperature, $J$ the heat flow in three directions, and the angle bracket represents the ensemble average. The heat flow $J$ is defined as

$$J = \sum v_i E_i + \sum_i \sum_{j \neq i} r_{ij} \left(\frac{\partial U_j}{\partial r_{ij}} \times v_i\right), \tag{5}$$

where $v_i$ and $E_i$ represent the velocity and the total energy of atom $i$, respectively. $U_j$ represents the potential energy of atom $j$, and $r_{ij}$ represents the position vector between the two atoms. The EMD simulations are carried out in a rectangular system with 960 atoms. The lattice thermal conductivity as a function of the number of atoms in the simulated system is presented in the Supplemental Material [33], which shows that there is no difference in the predicted thermal conductivity of a larger simulation system. The simulation is first performed on an ensemble with a fixed number of atoms, volume, and temperature for 800 ps to reach the system equilibrium. Then it is converted to another ensemble with a fixed number of atoms, volume, and energy, and another simulation is performed to collect the heat flow for 2 ns. Periodic boundary conditions are applied in all three directions and the time step is set as 2 fs. The average of 30 independent MD results is taken as the calculated value of thermal conductivity. Before each calculation of thermal conductivity, the equilibrium lattice constants are obtained by fully relaxing the supercell at the corresponding temperature. Since we do not try to consider the influence of quantum effects on the thermal conductivity and the Debye temperature of $Bi_2Te_3$ is 155 K [34], the thermal conductivity is calculated at temperatures above 150 K.

## III. RESULTS AND DISCUSSION

### A. Training and testing

In order to train a NNP, a training data set needs to be generated first. AIMD calculations at finite temperatures from 100 to 500 K and static self-consistent calculations for a lot of different degrees of perturbed structures are performed to obtain the information about system energy, atomic forces, and virial. Similarly, some defect structures with different native point defects are also calculated in the same operation to obtain the corresponding data set. Previous experimental research [35] and a first-principles study [36] showed that Te vacancy defects $V_{\text{Te}}$, and antisite defects $\text{Te}_{\text{Bi}}$ (Te at Bi site) or $\text{Bi}_{\text{Te}}$ (Bi at Te site) are dominant defects. Therefore, our data set contains the following five defects: antisite defects $\text{Bi}_{\text{Te1}}$, $\text{Bi}_{\text{Te2}}$, and $\text{Te}_{\text{Bi}}$; and vacancy defects $V_{\text{Te1}}$ and $V_{\text{Te2}}$. A total of about 15 000 snapshots are collected for the next step of potential training, including about 5500 snapshots for pure $Bi_2Te_3$ and about 9500 snapshots for different types of defect structures. All structures are rectangular supercells with 240 atoms. The detailed training process is shown in Sec. II.

To evaluate the quality of our potential, we compare the energy and force calculated by DFT and predicted with NNP. Like when acquiring the training data set, we perform static self-consistent calculations on 300 randomly perturbed $Bi_2Te_3$ snapshots and 300 defect snapshots, respectively, which are used as the testing data set. For pure $Bi_2Te_3$, the root-mean-square errors (RMSEs) of energy per atom and the atomic force are 0.218 meV/atom and 0.0216 eV/Å as shown in Figs. 1(a) and 1(b), while the RMSEs are 0.295 meV/atom and 0.0267 eV/Å for defect structures as shown in Figs. 1(c) and 1(d). Compared to the 35% and 210% force errors of the popular empirical potentials [37,38] for crystalline Si, the percentage relative

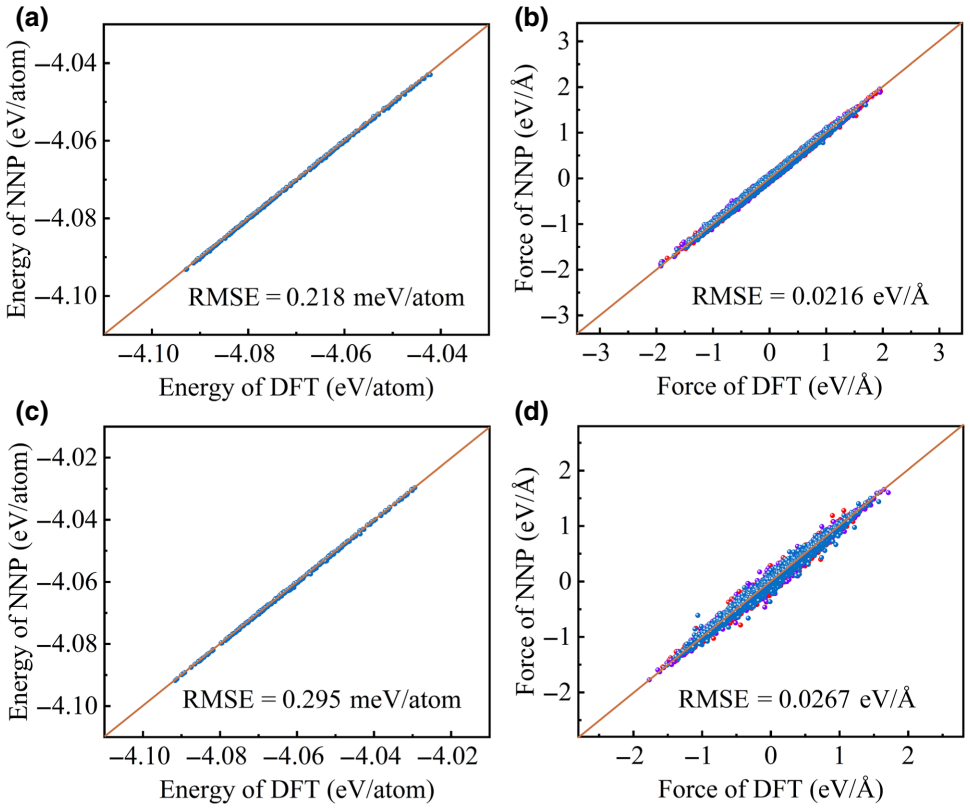


FIG. 1. Comparisons of energy per atom and atomic forces between NNP and DFT calculations for (a),(b) pure $Bi_2Te_3$ and (c),(d) five defect systems. The red dot, the purple dot, and the blue dot represent the forces in three directions of the atom.

absolute errors of this potential are only 3.96% and 4.79% for pure $Bi_2Te_3$ and defect structures, respectively, indicating that our potential is able to achieve as high precision as the DFT calculation.

### B. Structural properties and phonon dispersion with GGA + DFT-D3 functional

Lattice constants of bulk $Bi_2Te_3$ calculated with the LDA and GGA combined with various kinds of vdW functionals are listed in Table I. Among them, LDA and DFT-D3 are our calculation results. Experimental lattice constants and other calculated lattice constants are drawn from previous work [39,40]. It is obvious that the LDA functional tends to underestimate the lattice constants, which is consistent with the previously reported results [41]. Generally, the GGA is inclined to overestimate the lattice constants of the material, so it usually predicts the lattice constants of $Bi_2Te_3$ with a vdW correction. It should be mentioned that results calculated with the GGA + DFT-D3 functional are exceedingly close to experimental results, and also superior to any other vdW functionals.

Furthermore, we confirm that the GGA with DFT-D3 functional can reasonably describe the phonon dispersion of $Bi_2Te_3$ as well as the LDA. The LDA was verified to be capable of providing a better description of the phonon dispersion in $Bi_2Te_3$ than the GGA [41]. Almost all previously reported studies on thermal conductivity calculations for $Bi_2Te_3$ employed a LDA pseudopotential [8,10–12,41,42]. Hellman *et al.* [8] tested a series of vdW functionals to predict the phonon dispersion of $Bi_2Te_3$. However, all of them, namely vdW-DF [43], vdW-DF2 [44], optPBE-vdW, optB88-vdW, and optB86-vdW [45], underestimate the phonon frequencies. Li *et al.* [46] also reported the phonon dispersion of $Bi_2Te_3$ with the GGA + optB86b-vdW functional. Obviously, there was an underestimation in their reported phonon dispersion, especially in the *c*-axis direction Γ-*Z*. We compare the results of the GGA + DFT-D3, LDA, and experimental values [47] in Fig. 2. It is not hard to see that the GGA + DFT-D3 can describe phonon dispersion of $Bi_2Te_3$ as well as the LDA.

### C. Phonon thermal transport of pure $Bi_2Te_3$

We compare the phonon dispersions calculated by the NNP and empirical potential with the DFT calculation, as shown in Fig. 3(a). The phonon dispersion predicted by the Morse potential deviates substantially from the DFT calculations, especially for higher-frequency modes. In particular, there is a gap between 2 and 3 THz. Despite the fact that the optical phonons only have a small contribution to thermal conductivity due to the small group

TABLE I. Lattice constants of bulk $Bi_2Te_3$ calculated with LDA and GGA combined with various kinds of vdW functionals. Here $a_0$ and $\alpha$ describe the rhombohedral cell, while $a$ and $c$ describe the hexagonal cell. ($\pm u$, $\pm u$, $\pm u$) and ($\pm v$, $\pm v$, $\pm v$) are the internal coordinates of two Bi atoms and two Te1 atoms in a rhombohedral cell. $d$ is the interlayer distance between adjacent quantum layers.

| | Expt. | LDA | DFT-D2 | OptB86b-vdW | OptB88-vdW | OptPBE-vdW | VdW-DF2 | DFT-D3 |
|---|---|---|---|---|---|---|---|---|
| $a_0$ (Å) | 10.476 | 10.267 | 10.747 | 10.570 | 10.697 | 10.889 | 11.148 | 10.412 |
| $\alpha$ (deg) | 24.166 | 24.514 | 23.226 | 24.075 | 23.975 | 24.650 | 23.866 | 24.311 |
| $u$ (Bi) | 0.4000 | 0.4002 | 0.3984 | 0.3995 | 0.3992 | 0.3984 | 0.3988 | 0.4001 |
| $v$ (Te) | 0.2095 | 0.2089 | 0.2122 | 0.2106 | 0.2118 | 0.2135 | 0.2141 | 0.2092 |
| $a$ (Å) | 4.386 | 4.357 | 4.327 | 4.409 | 4.443 | 4.463 | 4.610 | 4.384 |
| $c$ (Å) | 30.497 | 29.939 | 31.357 | 30.778 | 31.153 | 31.741 | 32.477 | 30.285 |
| $d$ (Å) | 2.612 | 2.541 | 2.855 | 2.704 | 2.812 | 2.973 | 3.081 | 2.578 |

velocity, they indirectly affect the accuracy of the thermal conductivity calculation by affecting the phonon scattering process [9]. Consequently, the accurate prediction of optical-phonon modes is equally as crucial as the accurate prediction of acoustic-phonon modes. In contrast, the phonon dispersion predicted by the NNP is extremely consistent with those obtained by the DFT calculation in the whole frequency range, including the optical-phonon branches. Therefore, the NNP has an advantage over the empirical potential in predicting phonon transport behavior. Additionally, there are several common features in the phonon dispersion. First of all, they both share the characteristic of a degenerate state in the $c$-axis direction $\Gamma$-$Z$. Besides, it is not difficult to find that the three acoustic modes have a significantly lower slope in the out-of-plane direction than in-plane direction, suggesting that the in-plane phonon group velocity is larger compared with the out-of-plane one. This is the main reason why the in-plane thermal conductivity of $Bi_2Te_3$ is larger than the out-of-plane thermal conductivity.

Because of the weak chemical bonds in the tetradymite structures [48], the low phonon velocities may be one of the main reasons for the low intrinsic lattice thermal conductivity of $Bi_2Te_3$. Herein, the phonon velocities of three acoustic branches (including longitudinal (LA), in-plane transversal (TA), and out-of-plane (ZA) acoustic

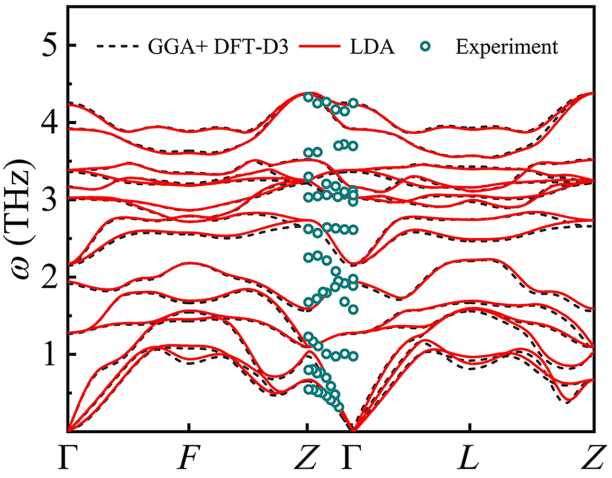


FIG. 2. The phonon dispersions calculated by GGA with DFT-D3 and LDA are compared with the experimental values. The black solid line represents the GGA with DFT-D3 calculation, the red dotted line represents the LDA calculation, and the green dot represents the experimental values.

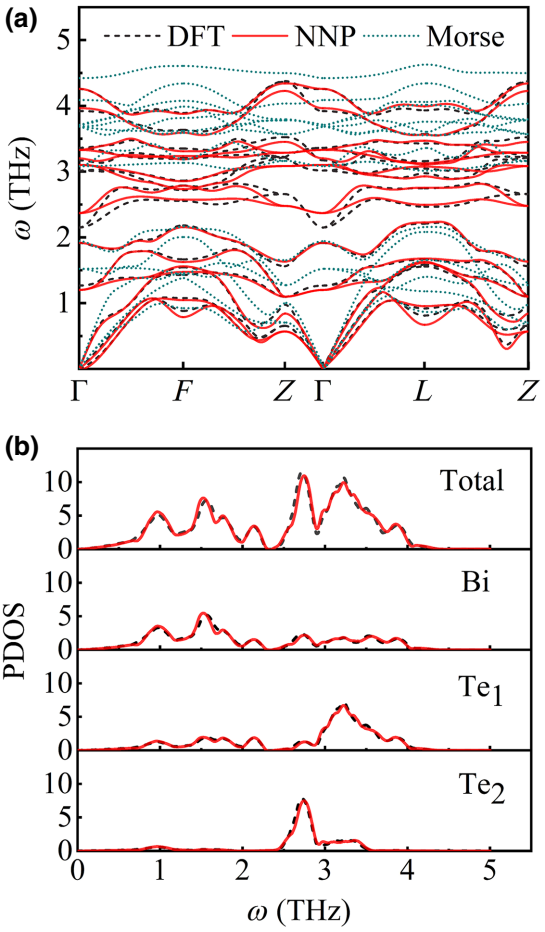


FIG. 3. (a) Phonon dispersions along high-symmetry paths and (b) partial phonon density of states (PDOS) for $Bi_2Te_3$. The black dotted line, red solid line, and green dotted line represent the predicted values of DFT, NNP, and Morse potential, respectively.

TABLE II. The calculated phonon velocities of three acoustic branches near the Γ point using DFT, NNP and traditional Morse potential. LA, TA and ZA in the table represent longitudinal, in-plane transversal, and out-of-plane acoustic branches, respectively.

| | Γ-*L* direction | | | Γ-*Z* direction | | |
|---|---|---|---|---|---|---|
| | $\upsilon_{LA}$ (m/s) | $\upsilon_{TA}$ (m/s) | $\upsilon_{ZA}$ (m/s) | $\upsilon_{LA}$ (m/s) | $\upsilon_{TA}$ (m/s) | $\upsilon_{ZA}$ (m/s) |
| LDA [41] | 2394 | 1728 | 1395 | 1811 | 1774 | 1774 |
| DFT | 2327 | 1682 | 1293 | 1879 | 1809 | 1789 |
| NNP | 2189 | 1607 | 1187 | 2423 | 1766 | 1756 |
| Morse | 2751 | 1862 | 1815 | 2452 | 1877 | 1877 |

branches) near the Γ point are estimated using DFT, NNP, and traditional Morse potential as listed in Table II. Firstly, the phonon velocities calculated by GGA + DFT-D3 are consistent with values predicted by the LDA pseudopotential reported in previous work [41], which further illustrates that the GGA with DFT-D3 functional can reasonably describe the phonon dispersion of $Bi_2Te_3$ as well as LDA. Turning to the phonon velocities calculated by NNP and Morse potential, except that $\upsilon_{LA}$ along the Γ-*Z* direction is significantly higher than value calculated by DFT, other results predicted by NNP are in good agreement with those of DFT, while the $\upsilon_{LA}$, $\upsilon_{zA}$ along the Γ-*L* direction and $\upsilon_{LA}$ along the Γ-*Z* direction predicted by Morse potential are all apparently larger than those predicted by DFT. Although the phonon velocities predicted by both the NNP and Morse potential are somewhat different from those of DFT in the very low frequency range (near the Γ point), it can be observed from phonon dispersion that they are equal to each other in a larger acoustic branch frequency range.

As for the phonon density of states, it is easily found that the results of DFT and NNP calculations are highly consistent as shown in Fig. 3(b). It is worth noting that the low-frequency acoustic modes are mainly dominated by the vibration of Bi atoms and the optical frequency range modes are dominated by the vibration of Te atoms. The atomic mass of Bi is larger than that of Te, and therefore a lower vibration frequency. The same phenomenon was also observed in another thermoelectric system, PbTe [49].

The anharmonicity is closely related to the scattering processes of phonons. To explore the anharmonicity of $Bi_2Te_3$, the three-phonon and four-phonon weighted phase spaces, which are related to the transition probabilities of phonon scattering processes, are calculated using the Fourphonon option of the SHENGBTE [50]. The weighted phase spaces calculated at 10, 300, and 500 K are shown in Fig. 4. Through the result at 10 K, we can find that three-phonon weighted phase space shows a broad peak in the medium frequency range, suggesting that three-phonon scattering processes play a major role at low temperatures, while the four-phonon scattering process can be ignored. When at or above room temperature, owing to the stronger scattering of phonons at higher temperatures, both the three-phonon and four-phonon weighted phase spaces are enhanced. In addition, differing from the case of low temperatures, the weighted phase spaces indicate that there are more channels for phonon scattering in the low-frequency region than the medium-frequency region at high temperatures. More importantly, it is not hard to find that the four-phonon weighted phase space is larger than the three-phonon weighted phase space, indicating that the four-phonon scattering processes have a great influence on the study of lattice thermal conductivity in $Bi_2Te_3$.

Next, we utilize the NNP combined with EMD simulation to predict the thermal conductivity of $Bi_2Te_3$. Figure 5(a) shows the representative normalized heat current autocorrelation function (HCACF) and the inset shows the thermal conductivities of $Bi_2Te_3$ at 300 K in two directions obtained by averaging 30 independent simulations. It can be seen that the correlation time of 100 ps is sufficient for thermal conductivity to reach convergence. At present, there are some studies on the lattice thermal conductivity of $Bi_2Te_3$. Because higher-order phonon scattering processes were not considered, the BTE method overestimated the thermal conductivity of the $Bi_2Te_3$ [10]. MD simulation inherently contains four-phonon scattering and higher-order scattering processes, so it is an effective method to calculate the thermal conductivity of materials with strong anharmonicity. Unfortunately, the inaccuracy of the empirical Morse potential in the MD simulation directly leads to the underestimate of thermal conductivity [12]. The fundamental reason is that this potential is unable to ideally reproduce the optical branches of the phonon dispersion as described previously. Our MD simulations with a NNP theoretically possess as high accuracy as DFT. As a consequence, our calculated results are in great agreement with the experimental results [51,52] in the temperature range of 150 to 450 K as shown in Fig. 5(b). Additionally, as a validation, we develop a deep-neural-network interatomic potential with LDA pseudopotential using the same method, and find that it can also accurately predict the thermal conductivity of $Bi_2Te_3$, as shown in the Supplemental Material [33].

### D. The effects of native point defects on thermal conductivity in $Bi_2Te_3$

In order to further show that the NNP can predict the energy of defect structures as well as DFT calculations, we calculate the defect formation energies using DFT and the

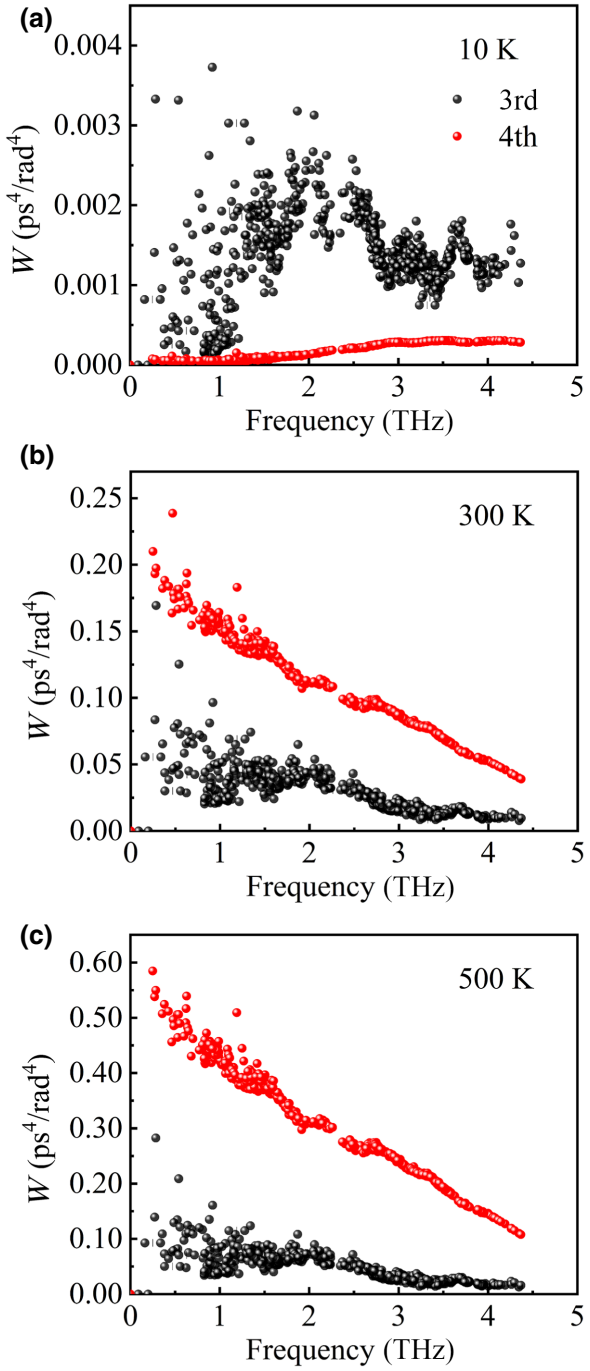


FIG. 4. The calculated three-phonon and four-phonon weighted phase spaces of pure $Bi_2Te_3$ at 10, 300, and 500 K, respectively.

NNP, respectively. The formation energy $\Delta H_f$ of a point defect is defined as [53]

$$\Delta H_f = E_{\text{tot}} - E_{\text{bulk}} - \sum_i \Delta n_i \mu_i + q(E_f + E_V + \Delta V), \tag{6}$$

where $E_{\text{tot}}$ and $E_{\text{bulk}}$ represent the total energies of the host material with and without defects, respectively. $\mu_i$ and $\Delta n_i$ denote the chemical potential and the change of the number of elements $i$. The last term is used to correct the change in energy due to the charge state of the defect. Here we only consider charge neutral defects and neglect this correction term. As for $Bi_2Te_3$, the chemical potentials of Bi ($\mu_{\text{Bi}}$) and Te ($\mu_{\text{Te}}$) depend on the growth environment, whether it is in the Bi-rich state or the Te-rich state. At the same time, their values should be smaller than the chemical potentials of solid Bi ($\mu_{\text{Bi}}^{\text{solid}}$) and Te ($\mu_{\text{Te}}^{\text{solid}}$) to prevent the overflow of the solid elemental phase in the compound. The relationship between them satisfies the following:

$$\mu_{\text{bulk}} = 2\mu_{\text{Bi}} + 3\mu_{\text{Te}}, \tag{7}$$

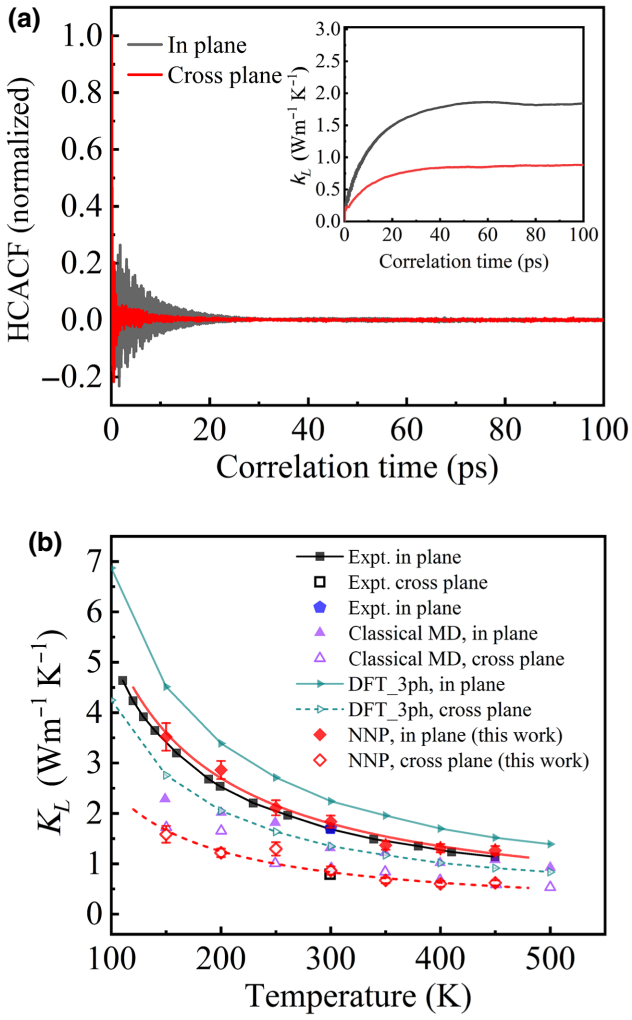


FIG. 5. (a) The representative normalized HCACF of in-plane and out-of-plane directions. The inset shows thermal conductivities of $Bi_2Te_3$ in two different directions as a function of correlation time at 300 K, each of which is the average value of 30 independent simulations. (b) Temperature-dependent thermal conductivity of $Bi_2Te_3$ predicted by NNP, compared with experimental values (Refs. [51,52]) and results calculated by classical MD (Ref. [12]) and DFT (Ref. [10]).

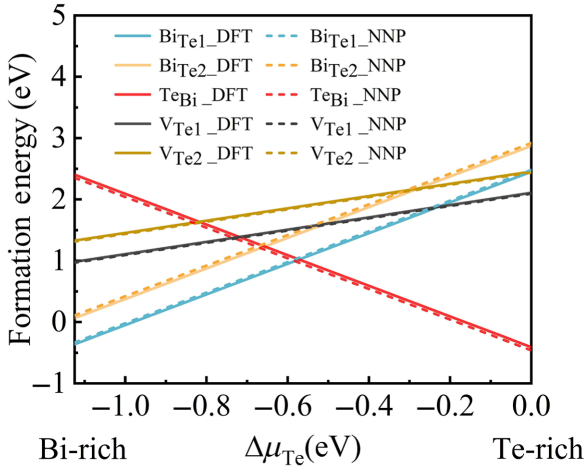


FIG. 6. The formation energies as a function of $\Delta\mu_{Te}$ for the five intrinsic defects in $Bi_2Te_3$. The solid line represents the calculated results of DFT and the dotted line represents the predicted results of NNP.

$$\mu_{Bi} = \Delta\mu_{Bi} + \mu_{Bi}^{solid}, \tag{8}$$

$$\mu_{Te} = \Delta\mu_{Te} + \mu_{Te}^{solid}, \tag{9}$$

$$\mu_{bulk} = 2\mu_{Bi}^{solid} + 3\mu_{Te}^{solid} + 2\Delta\mu_{Bi} + 3\Delta\mu_{Te}. \tag{10}$$

Thus, we can present the formation energy as a function of $\Delta\mu_{Te}$ $((\mu_{bulk} - 2\mu_{Bi}^{solid} - 3\mu_{Te}^{solid})/3 \leq \Delta\mu_{Te} \leq 0)$. A hexagonal $4 \times 4 \times 1$ conventional supercell is used to calculate the formation energies of various defects.

Figure 6 shows the formation energies of five types of defects. The errors of defect formation energies predicted by the NNP for these five defect structures are 0.029, 0.045, 0.051, 0.015, and 0.016 eV, respectively, indicating that the NNP is able to predict the energies of defect structures as well as DFT. According to the results, antisite defects are prominent defects. $Bi_{Te}$ and $Te_{Bi}$ are easily generated in Bi-rich and Te-rich environments, respectively. Our finding is consistent with the results previously reported [36]. An experimental study showed that Te vacancies $V_{Te}$ are another dominant defects besides the antisite defects of $Te_{Bi}$ and $Bi_{Te}$ [35]. This may be attributed to the fact that the formation energy of Te vacancy defects is close to that of antisite defects. As a result, Te vacancies may also easily come into being in the real environment. To explore the effects of intrinsic defects on thermal conductivity, we consider the following five types of defects: antisite defects $Bi_{Te1}$, $Bi_{Te2}$, and $Te_{Bi}$; and vacancy defects $V_{Te1}$ and $V_{Te2}$.

Figure 7 shows the thermal conductivities of structures with different defect types and concentrations (1 defect, 4 defects, 8 defects, and 12 defects per 960 atoms,

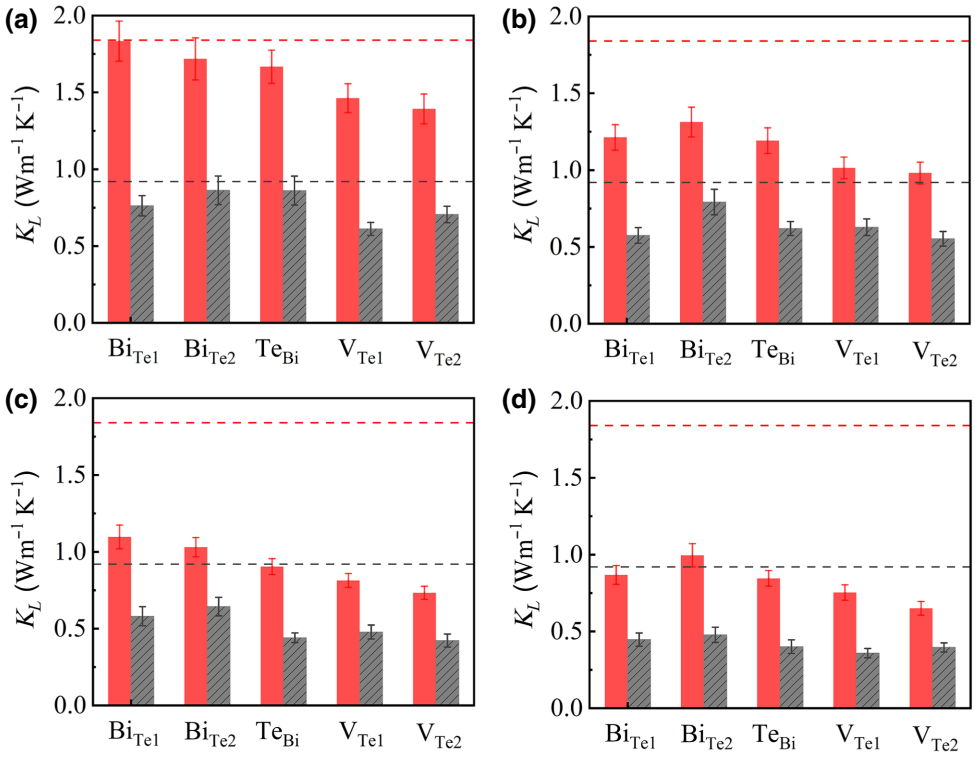


FIG. 7. The thermal conductivities of five different defect structures at 300 K with different defect concentrations. The defect concentrations are about (a) 1‰, (b) 4‰, (c) 8‰, and (d) 12.5‰, respectively. The red (black) bars show the thermal conductivities of defect structures in the in-plane (cross-plane) direction, and the red (black) dashed line represents the thermal conductivity of the perfect $Bi_2Te_3$ in the in-plane (cross-plane) direction.

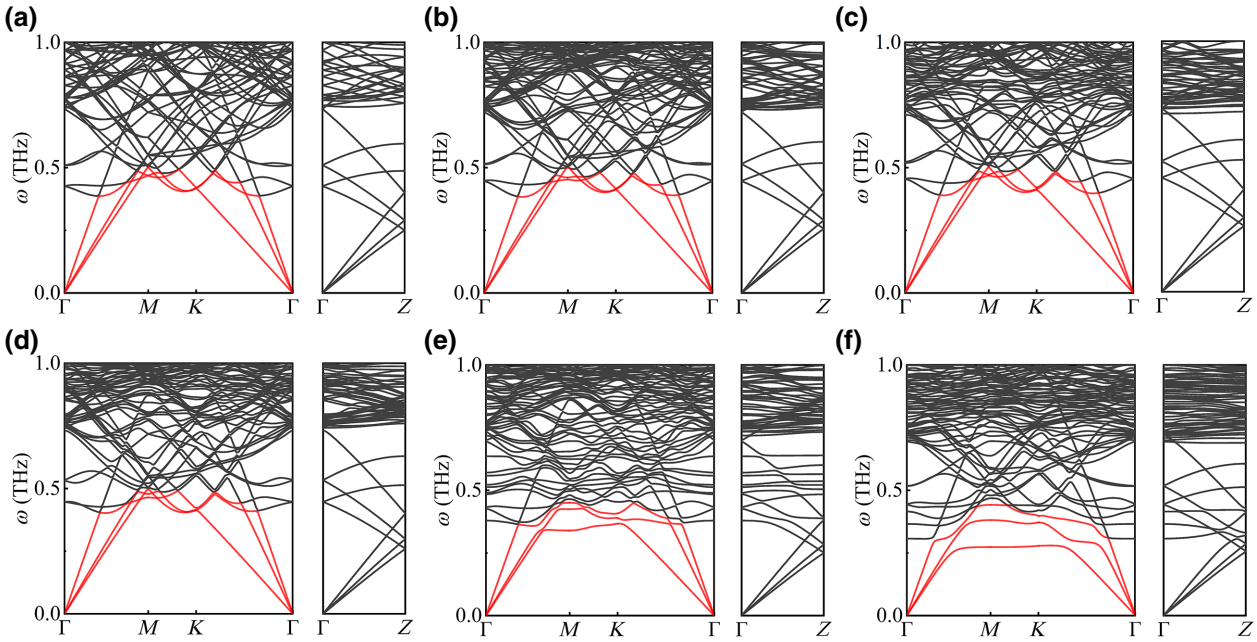


FIG. 8. Phonon dispersions of (a) pure $Bi_2Te_3$ and five defect structures: (b) $Bi_{Te1}$, (c) $Bi_{Te2}$, (d) $Te_{Bi}$, (e) $V_{Te1}$, and (f) $V_{Te2}$.

respectively) at 300 K. Apparently, due to the scattering between defects and phonons, the thermal conductivities of all defect-containing structures decrease in varying degrees compared with pure $Bi_2Te_3$. Meanwhile, when comparing the thermal conductivities of structures with a certain defect type but different defect concentrations, it is not difficult to find that the thermal conductivities decrease with the increase of defect concentration, which can be attributed to the enhancement of phonon scattering with the increase of defect concentration. In addition, it is interesting to find that Te vacancies $V_{Te}$ play a most significant role in reducing the thermal conductivity. To uncover the reason, we further calculate the phonon dispersion curves of perfect $Bi_2Te_3$ and $Bi_2Te_3$ with different kinds of defects using the obtained NNP. Figure 8 shows the phonon dispersions in the in-plane and out-of-plane directions. Because low-frequency acoustic phonons play a decisive role in heat transfer in $Bi_2Te_3$, we only show the phonon dispersions below 1 THz. The difference of phonon dispersions between the three defect structures ($Bi_{Te1}$, $Bi_{Te2}$, and $Te_{Bi}$) and the pure $Bi_2Te_3$ is not obvious. However, the phonon dispersions of the Te vacancy defect structures, interestingly, are found to be quite different from those of the others. In the in-plane direction, the frequency of the acoustic phonons is reduced, and the tops of some acoustic branches are quite flat, especially for $V_{Te2}$, implying that the Te vacancies hinder the propagation of phonons in the in-plane direction and lead to lower phonon velocity. This may be attributed to the reduction of strength of the chemical bonds of atoms around the vacancies. The same phenomenon is also observed in $In_4Se_{3-x}$, where Se vacancies strongly suppress the propagation velocity of phonons along the chain direction and lead to an extremely low thermal conductivity [54]. In the out-of-plane direction, acoustic phonons and low-frequency optical phonons have decisive contributions to thermal conductivity due to large phonon velocity. Although there is no obvious change in the acoustic modes for all types of defects, detectable changes are observed in optical modes. Some optical modes shift to lower frequency region in the Te vacancy defect structures. The velocity of the downward moving optical phonons does not change significantly because the slopes are almost unchanged compared with the high-frequency optical modes. However, the downward shift of some optical modes produces additional scattering among original low-frequency optical phonons and the fresh low-frequency optical phonons moving downward from high frequency region, and thus lower the thermal conductivity in the $z$-axis direction. In conclusion, the stronger phonon scattering caused by defects is responsible for the reduced thermal conductivity of all native point defect structures. Moreover, the most significant reduction of thermal conductivity by Te vacancies may be attributed to the reduction of the phonon velocity and the enlargement of scattering among low-frequency optical phonons.

The accurate calculation of the lattice thermal conductivity of $Bi_2Te_3$ is a challenging task due to its strong anharmonicity and complex crystal structure. Because of the strong anharmonicity of the $Bi_2Te_3$, it is necessary to consider the fourth-order or even higher-order phonon scattering processes in the calculation of its lattice thermal

conductivity, but it is extremely time consuming to obtain the fourth-order force constants using DFT. Owing to its complex crystal structure, the fitting of an empirical potential used in MD simulations is often difficult and imprecise. The preceding results show that, inherently containing full order anharmonicity and possessing precision as high as DFT calculations, the MD simulations with the NNP are able to accurately reproduce the experimental lattice thermal conductivity of $Bi_2Te_3$. More importantly, it is difficult to explore the effects of nanostructures, such as defects, superlattices, twins, dislocations, etc, on thermal conductivity in $Bi_2Te_3$. The effects of the native point defects on the thermal conductivity are also discussed in this work using MD simulations with a NNP, which provides a feasible method to explore the influence of nanostructures on thermal conductivity.

## IV. CONCLUSION

In summary, a NNP for $Bi_2Te_3$ is developed to predict its thermal transfer behavior. The phonon dispersion and phonon density of states are in great agreement with the DFT calculation. The thermal conductivity values predicted by the NNP are found to be highly consistent with the experimental values in the whole temperature range. In addition, we find that the GGA with DFT-D3 functional can accurately reproduce the experimental lattice constants of $Bi_2Te_3$ and provide a great description of the phonon dispersion in $Bi_2Te_3$. A NNP trained with a LDA pseudopotential is also developed, which can similarly predict the thermal conductivity of $Bi_2Te_3$. Furthermore, an investigation of the influences of several different intrinsic point defects on the thermal conductivity of $Bi_2Te_3$ shows that Te vacancies decrease the thermal conductivity most significantly, which can be attributed to the reduction of the propagation velocity of phonons and additional scattering among original low-frequency optical phonons and the fresh low-frequency optical phonons moving downward from high frequency region. Our work demonstrates that EMD simulation combined with a NNP is able to calculate the thermal conductivity of materials with strong anharmonicity and provides a tool for studying the influence of some nanostructures on thermal conductivity. Additionally, the NNP developed in this work can also be utilized to study some other properties of $Bi_2Te_3$, such as mechanical and thermomechanical properties.

## ACKNOWLEDGMENTS

This work is supported by the National Natural Science Foundation of China (Grant No. 91963207) and Suzhou Key Industrial Technology Innovation Project (Grant No. SYG201921). We also thank support from the Supercomputing Center of Wuhan University, and all numerical calculations in this paper have been done on the supercomputing system.

[1] L. E. Bell, Cooling, heating, generating power, and recovering waste heat with thermoelectric systems, Science **321**, 1457 (2008).

[2] J. He and T. M. Tritt, Advances in thermoelectric materials research: Looking back and moving forward, Science **357**, eaak9997 (2017).

[3] B. Poudel, Q. Hao, Y. Ma, Y. C. Lan, A. Minnich, B. Yu, X. Yan, D. Z. Wang, A. Muto, D. Vashaee, *et al.*, High-thermoelectric performance of nanostructured bismuth antimony telluride bulk alloys, Science **320**, 634 (2008).

[4] S. I. Kim, K. H. Lee, H. A. Mun, H. S. Kim, S. W. Hwang, J. W. Roh, D. J. Yang, W. H. Shin, X. S. Li, Y. H. Lee, *et al.*, Dense dislocation arrays embedded in grain boundaries for high-performance bulk thermoelectrics, Science **348**, 109 (2015).

[5] R. Venkatasubramanian, Lattice Thermal Conductivity Reduction and Phonon Localizationlike Behavior in Superlattice Structures, Phys. Rev. B **61**, 3091 (2000).

[6] R. Venkatasubramanian, E. Siivola, T. Colpitts, and B. O'Quinn, Thin-film thermoelectric devices with high room-temperature figures of merit, Nature **413**, 597 (2001).

[7] K. Biswas, J. He, I. D. Blum, C.-I. Wu, T. P. Hogan, D. N. Seidman, V. P. Dravid, and M. G. Kanatzidis, High-performance bulk thermoelectrics with all-scale hierarchical architectures, Nature **489**, 414 (2012).

[8] O. Hellman and D. A. Broido, Phonon thermal transport in $Bi_2Te_3$ from first principles, Phys. Rev. B **90**, 134309 (2014).

[9] Y. Ouyang, C. Yu, J. He, P. Jiang, W. Ren, and J. Chen, Accurate description of high-order phonon anharmonicity and lattice thermal conductivity from molecular dynamics simulations with machine learning potential, Phys. Rev. B **105**, 115202 (2022).

[10] A. Jena, S. C. Lee, and S. Bhattacharjee, Tuning the Lattice Thermal Conductivity in Bismuth Telluride via Cr Alloying, Phys. Rev. Appl. **15**, 064023 (2021).

[11] B.-L. Huang and M. Kaviany, Ab initio and molecular dynamics predictions for electron and phonon transport in bismuth telluride, Phys. Rev. B **77**, 125209 (2008).

[12] B. Qiu and X. Ruan, Molecular dynamics simulations of lattice thermal conductivity of bismuth telluride using two-body interatomic potentials, Phys. Rev. B **80**, 165203 (2009).

[13] H. J. Goldsmid, The thermal conductivity of bismuth telluride, Proc. Phys. Soc. B **69**, 203 (1956).

[14] H. Wang, L. Zhang, J. Han, and W. E, DeePMD-Kit: A deep learning package for many-body potential energy representation and molecular dynamics, Comput. Phys. Commun. **228**, 178 (2018).

[15] A. P. Bartók, M. C. Payne, R. Kondor, and G. Csányi, Gaussian Approximation Potentials: The Accuracy of Quantum Mechanics, without the Electrons, Phys. Rev. Lett. **104**, 136403 (2010).

[16] G. P. P. Pun, R. Batra, R. Ramprasad, and Y. Mishin, physically informed artificial neural networks for atomistic modeling of materials, Nat. Commun. **10**, 2339 (2019).

[17] Z. Fan, Z. Zeng, C. Zhang, Y. Wang, H. Dong, Y. Chen, and T. Ala-Nissila, Neuroevolution machine learning potentials: Combining high accuracy and low cost in atomistic simulations and application to heat transport, Phys. Rev. B **104**, 104309 (2021).

[18] I. S. Novikov, K. Gubaev, E. V. Podryabinkin, and A. V. Shapeev, The MLIP package: Moment tensor potentials with MPI and active learning, Mach. Learn.: Sci. Technol. **2**, 025002 (2021).

[19] R. Li, Z. Liu, A. Rohskopf, K. Gordiz, A. Henry, E. Lee, and T. Luo, A deep neural network interatomic potential for studying thermal conductivity of $\beta$-$Ga_2O_3$, Appl. Phys. Lett. **117**, 152102 (2020).

[20] C. Mangold, S. Chen, G. Barbalinardo, J. Behler, P. Pochet, K. Termentzidis, Y. Han, L. Chaput, D. Lacroix, and D. Donadio, Transferability of neural network potentials for varying stoichiometry: Phonons and thermal conductivity of Mn*x*Ge*y* compounds, J. Appl. Phys. **127**, 244901 (2020).

[21] X. Qian, S. Peng, X. Li, Y. Wei, and R. Yang, Thermal conductivity modeling using machine learning potentials: Application to crystalline and amorphous silicon, Mater. Today Phys. **10**, 100140 (2019).

[22] R. Li, E. Lee, and T. Luo, A unified deep neural network potential capable of predicting thermal conductivity of silicon in different phases, Mater. Today Phys. **12**, 100181 (2020).

[23] G. Pan, J. Ding, Y. Du, D.-J. Lee, and Y. Lu, A DFT accurate machine learning description of molten $ZnCl_2$ and its mixtures: 2. Potential development and properties prediction of $ZnCl_2$-NaCl-KCl ternary salt for CSP, Comput. Mater. Sci. **187**, 110055 (2021).

[24] P. Korotaev, I. Novoselov, A. Yanilkin, and A. Shapeev, Accessing thermal conductivity of complex compounds by machine learning interatomic potentials, Phys. Rev. B **100**, 144308 (2019).

[25] P. Korotaev and A. Shapeev, Lattice Dynamics of $Yb_xCo_4Sb_{12}$ Skutterudite by machine-learning interatomic potentials: Effect of filler concentration and disorder, Phys. Rev. B **102**, 184305 (2020).

[26] G. Kresse and J. Furthmüller, Efficient iterative schemes for ab initio total-energy calculations using a plane-wave basis set, Phys. Rev. B **54**, 11169 (1996).

[27] P. E. Blochl, Projector augmented-wave method, Phys. Rev. B **50**, 17953 (1994).

[28] J. P. Perdew, K. Burke, and M. Ernzerhof, Generalized Gradient Approximation Made Simple, Phys. Rev. Lett. **77**, 3865 (1996).

[29] S. Grimme, J. Antony, S. Ehrlich, and H. Krieg, A consistent and accurate ab initio parametrization of density functional dispersion correction (DFT-D) for the 94 elements H-Pu, J. Chem. Phys. **132**, 154104 (2010).

[30] L. Chaput, A. Togo, I. Tanaka, and G. Hug, Phonon-phonon interactions in transition metals, Phys. Rev. B **84**, 094302 (2011).

[31] P. K. Schelling, S. R. Phillpot, and P. Keblinski, Comparison of atomic-level simulation methods for computing thermal conductivity, Phys. Rev. B **65**, 144306 (2002).

[32] S. Plimpton, Fast parallel algorithms for short-range molecular dynamics, J. Comput. Phys. **117**, 1 (1995).

[33] See Supplemental Material at http://link.aps.org/supplemental/10.1103/PhysRevApplied.18.054022 for the lattice thermal conductivity as a function of the number of atoms in the simulated system and a deep-neural-network interatomic potential with LDA pseudopotential.

[34] G. E. Shoemake, J. A. Rayne, and R. W. Ure, Jr., Specific heat of *n*- and *p*-type $Bi_2Te_3$ from 1.4 to 90'K, Phys. Rev. **185**, 1046 (1969).

[35] M. Zhang, W. Liu, C. Zhang, S. Xie, Z. Li, F. Q. Hua, J. F. Luo, Z. H. Wang, W. Wang, F. Yan, *et al.*, Identifying the manipulation of individual atomic-scale defects for boosting thermoelectric performances in artificially controlled $Bi_2Te_3$ films, ACS Nano **15**, 5706 (2021).

[36] A. Hashibon and C. Elsässer, First-Principles Density Functional Theory Study of Native Point Defects in $Bi_2Te_3$, Phys. Rev. B **84**, 144117 (2011).

[37] J. Tersoff, Modeling solid-state chemistry: Interatomic potentials for multicomponent systems, Phys. Rev. B **39**, 5566 (1988).

[38] F. H. Stillinger and T. A. Weber, Computer simulation of local order in condensed phases of silicon, Phys. Rev. B **31**, 5262 (1985).

[39] L. Cheng, H. J. Liu, J. Zhang, J. Wei, J. H. Liang, J. Shi, and X. F. Tang, Effects of van der Waals interactions and quasiparticle corrections on the electronic and transport properties of $Bi_2Te_3$, Phys. Rev. B **90**, 085118 (2014).

[40] S. Nakajima, The lattice structure of $Bi_2Te_3$, J. Phys. Chem. Solids **24**, 479 (1963).

[41] X. Chen, D. Parker, and D. J. Singh, Acoustic impedance and interface phonon scattering in $Bi_2Te_3$ and other semiconducting materials, Phys. Rev. B **87**, 045317 (2013).

[42] T. Fang, X. Li, C. Hu, Q. Zhang, J. Yang, W. Zhang, X. Zhao, D. J. Singh, and T. Zhu, Complex band structures and lattice dynamics of $Bi_2Te_3$-based compounds and solid solutions, Adv. Funct. Mater. **29**, 1900677 (2019).

[43] M. Dion, H. Rydberg, E. Schröder, D. C. Langreth, and B. I. Lundqvist, Van der Waals Density Functional for General Geometries, Phys. Rev. Lett. **92**, 246401 (2004).

[44] K. Lee, É. D. Murray, L. Kong, B. I. Lundqvist, and D. C. Langreth, Higher-accuracy van der Waals density functional, Phys. Rev. B **82**, 081101 (2010).

[45] J. Klimeš, D. R. Bowler, and A. Michaelides, Chemical accuracy for the van der Waals density functional, J. Phys.: Condens. Matter **22**, 022201 (2010).

[46] M. K. Li, C. Y. Sheng, R. Hu, S. H. Han, H. M. Yuan, and H. J. Liu, Effects of van der Waals interactions on the phonon transport properties of tetradymite compounds, New J. Phys. **23**, 083002 (2021).

[47] W. Kullmann, G. Eichhorn, H. Rauh, R. Geick, G. Eckold, and U. Steigenberger, Lattice dynamics and phonon dispersion in the narrow gap semiconductor $Bi_2Te_3$ with sandwich structure, Phys. Status Solidi B **162**, 125 (1990).

[48] N. T. Hung, A. R. T. Nugraha, and R. Saito, Designing high-performance thermoelectrics in two-dimensional tetradymites, Nano Energy **58**, 743 (2019).

[49] B. Qiu, H. Bao, G. Zhang, Y. Wu, and X. Ruan, Molecular dynamics simulations of lattice thermal conductivity

and spectral phonon mean free path of PbTe: Bulk and nanostructures, Comput. Phys. Commun. **53**, 278 (2012).

[50] Z. Han, X. Yang, W. Li, T. Feng, and X. Ruan, FourPhonon: An extension module to ShengBTE for computing four-phonon scattering rates and thermal conductivity, Comput. Phys. Commun. **270**, 108179 (2022).

[51] C. B. Satterthwaete and J. R. W. Ure, Electrical and thermal properties of $Bi_2Te_3$, Phys. Rev. **108**, 1164 (1957).

[52] J. P. Fleurial, L. Gailliard, R. Triboulet, H. Scherrer, and S. Scherrer, Thermal properties of high quality single crystals of bismuth telluride—Part I: Experimental characterization, J. Phys. Chem. Solids **49**, 1237 (1988).

[53] C. G. Van de Walle and J. Neugebauer, First-principles calculations for defects and impurities: Applications to III-nitrides, J. Appl. Phys. **95**, 3851 (2004).

[54] H. S. Ji, H. Kim, C. Lee, J.-S. Rhyee, M. H. Kim, M. Kaviany, and J. H. Shim, Vacancy-suppressed lattice conductivity of high-$ZT$ $In_4Se_{3-x}$, Phys. Rev. B **87**, 125111 (2013).